Supplementary Information

Relating the thermodynamic warming response of precipitation and streamflows across the contiguous United States

Marc Prange, Ming Zhao, Elena Shevliakova, Sergey Malyshev, Minki Hong

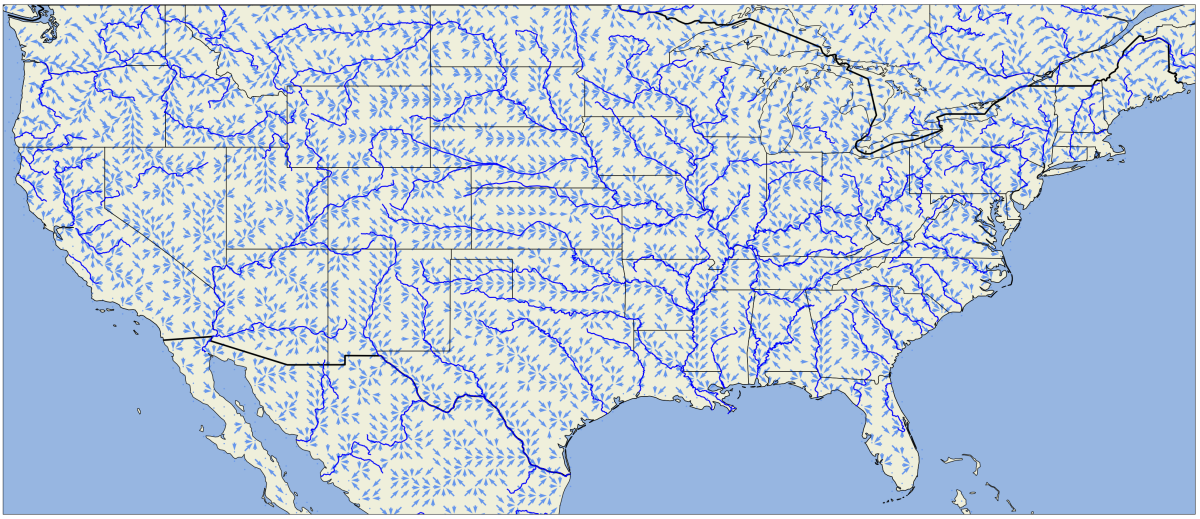

Figure S1: Grid-scale river network of AM4.0/LM4.0 that discharges runoff to the ocean following Milly et al. (2014). The blue arrows denote the 8-connectivity streamflow direction. The blue lines denote major river streams from the Natural Earth Database(https://www.naturalearthdata.com, last access: 03/20/2025).

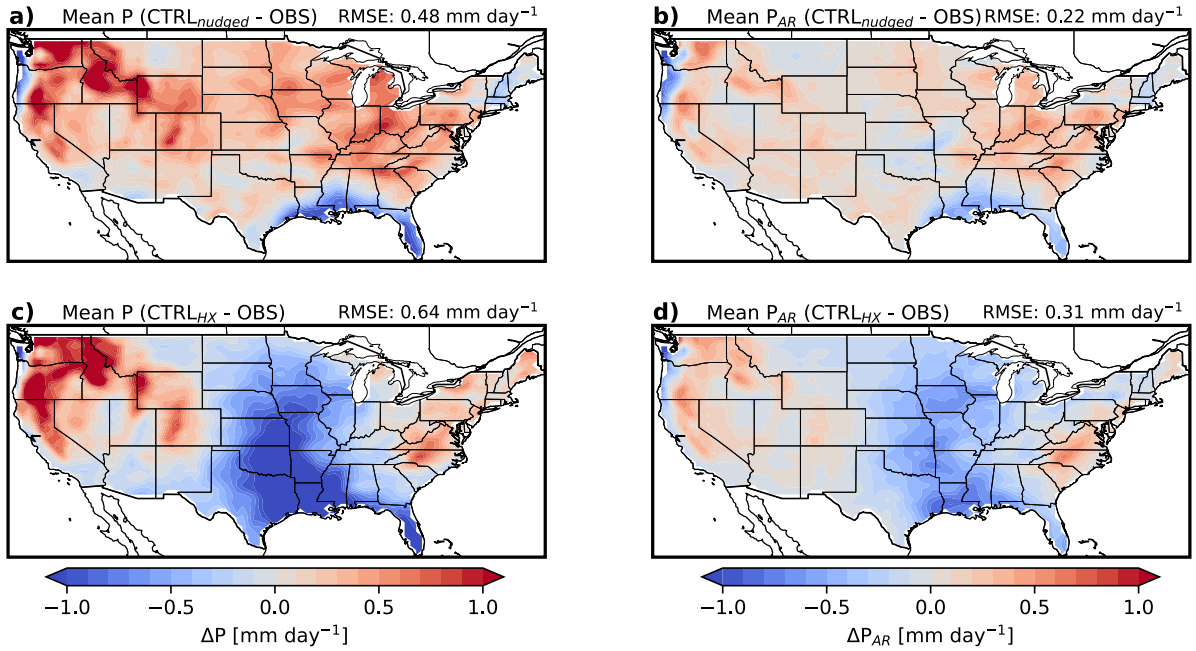

Figure S2: Climatological biases in mean precipitation (a+c) and AR precipitation (b+d) between nudged CTRL simulation and IMERG observations (a+b) and between free run CTRL simulation and IMERG (c+d). AR detection for IMERG dataset is done based on IVT deduced from ERA5. Dry bias over central US in free run CTRL simulations are mostly resolved in nudged simulations. Overall, reduction of RMSE is found for both P and P_{AR} in nudged simulations.

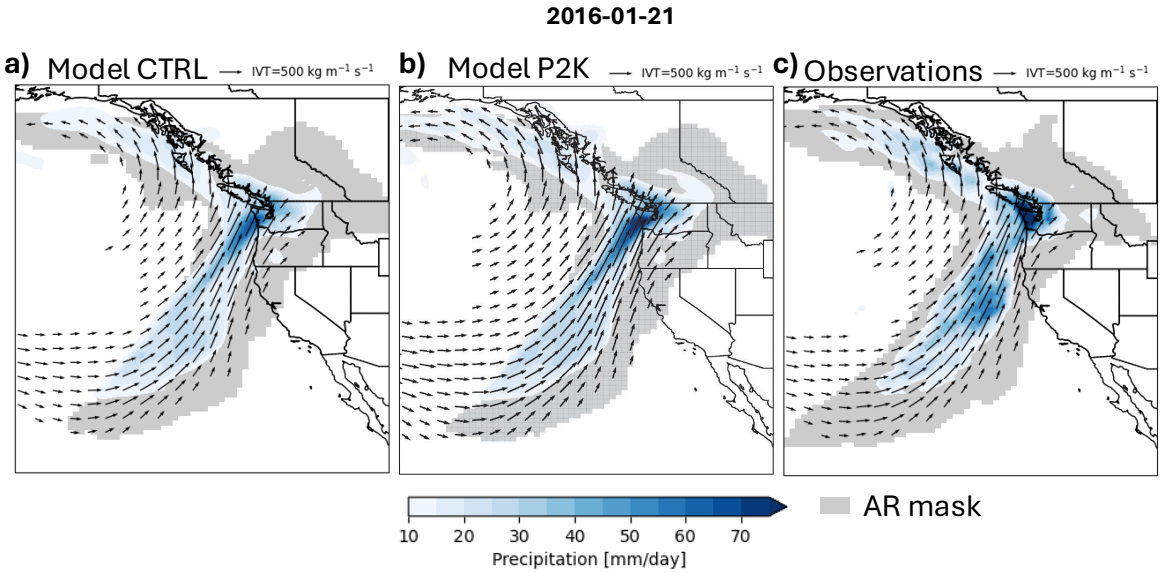

Figure S3: Snapshot of an Atmospheric River on 2016-01-21 over the Western US in the CTRL simulation (a), P2K simulation (b) and in Observations (c). Observations are based on ERA5 for IVT and the derived AR mask and IMERG for precipitation.

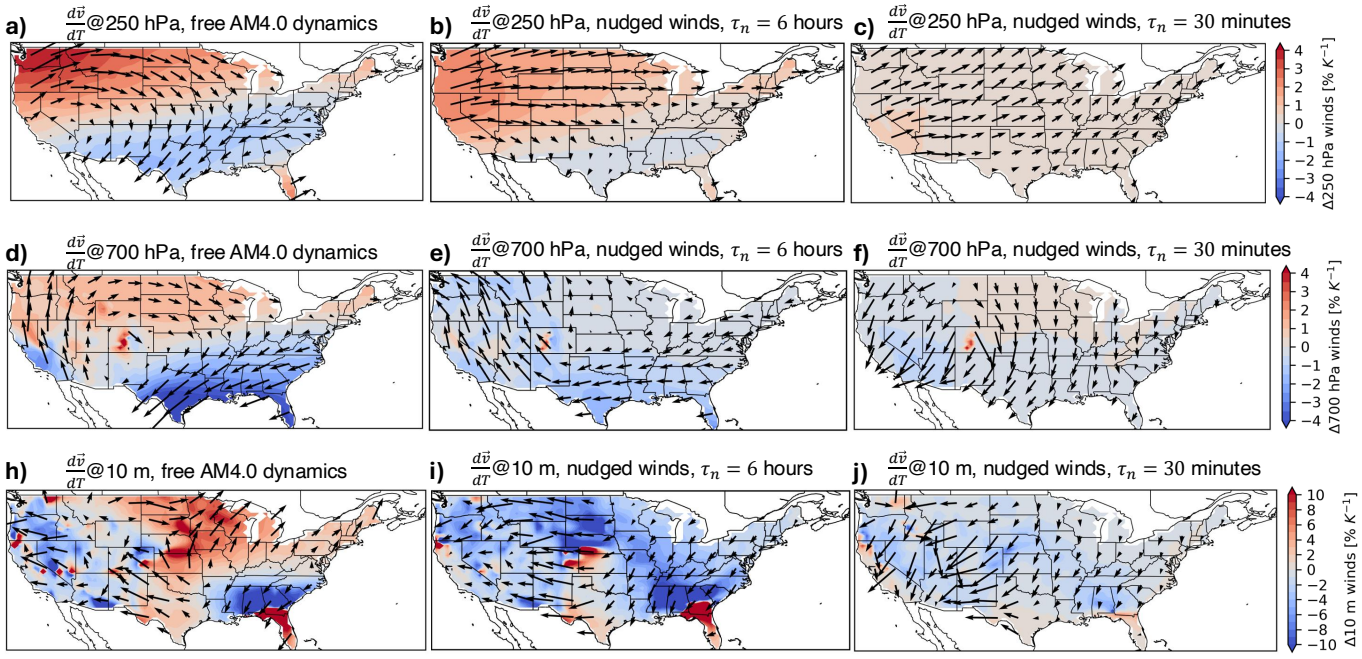

Figure S4: Changes in atmospheric winds with warming at 250 hPa (first row), 700 hPa (second row) and at 10 m above ground (third row) for three different sets of CTRL and P2K warming experiments. The first experiment uses AM4.0 with unconstrained atmospheric dynamics, i.e. without nudging (first column), in the second experiment atmospheric winds are against NCEP reanalysis with a nudging timescale τ_n of 6 hours (second column), and in the third experiment τ_n is reduced to 30 minutes (third column).

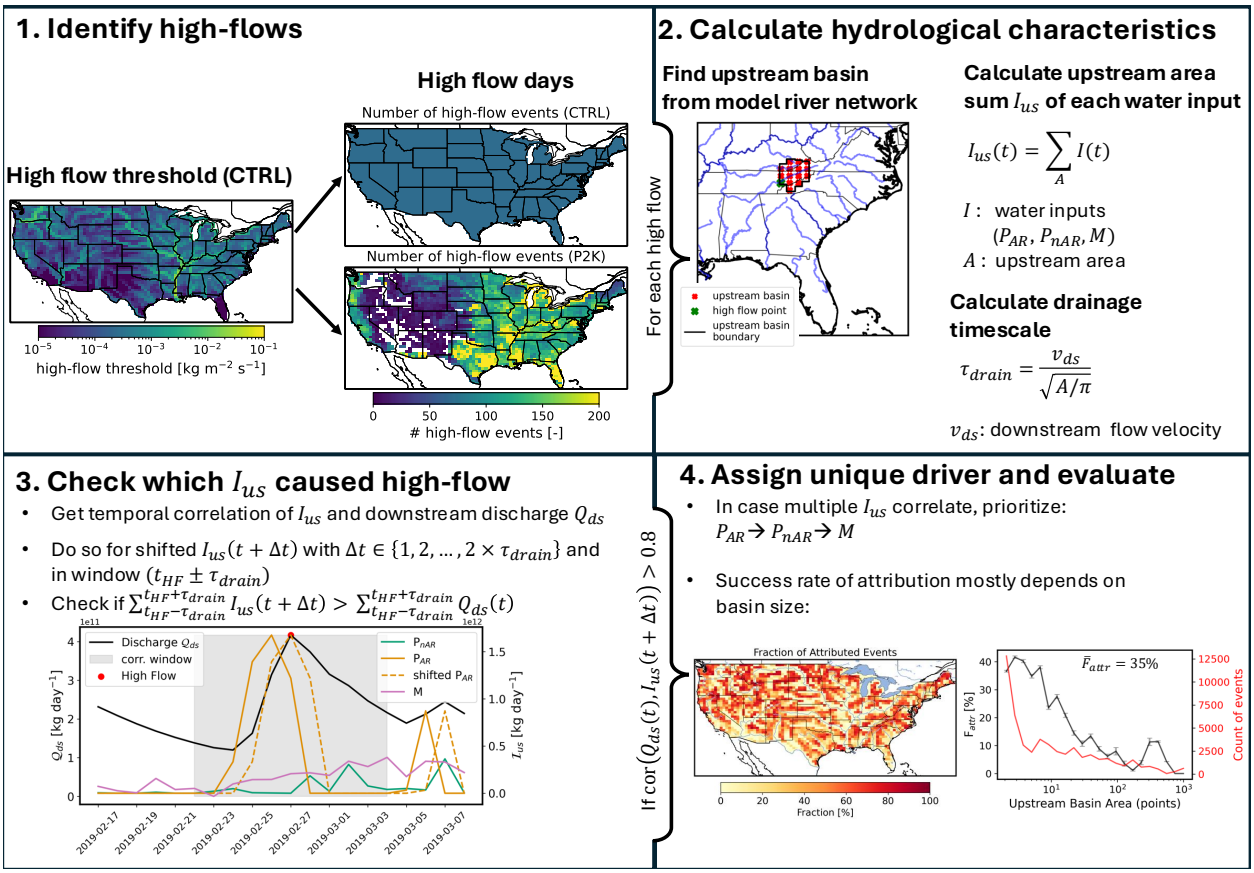

Figure S5: Workflow of high-flow attribution method. First, high-flows are identified using the 99.7th percentile of the 70 year timeseries of daily streamflows at each grid-point of the CTRL simulation as a threshold for the CTRL and the P2K simulation, resulting in 70 identified high-flow events at each grid-point in the CTRL simulation and a varying number of events in the P2K simulation. Secondly, for each high-flow event, the upstream river basin is identified and the area sum of different upstream water sources is calculated, distinguishing AR precipitation, non-AR precipitation and melt. A drainage timescale is calculated using the downstream flow-velocity and the upstream basin area. In a third step, the timeseries of upstream water sources and downstream streamflow are temporally correlated within a temporal window around the high-flow day, which is set by the drainage timescale. In addition, the timeseries of upstream water sources is shifted by by a varying number of days that ranges between 1 and twice the drainage timescale. If for any of these lagged correlation analyses a correlation coefficient > 0.8 is found for any of the upstream water sources, we consider this water source the upstream driver of the high-flow. Step 4 summarizes an evaluation of the method, when applied to the CTRL simulation, showing a map of the fraction of successfully attributed events to the total number of high-flow events and a line plot showing the dependence of the attribution rate on the upstream basin size. The method is able to attribute 35 % of all high-flow cases, and performs best for small river basins.

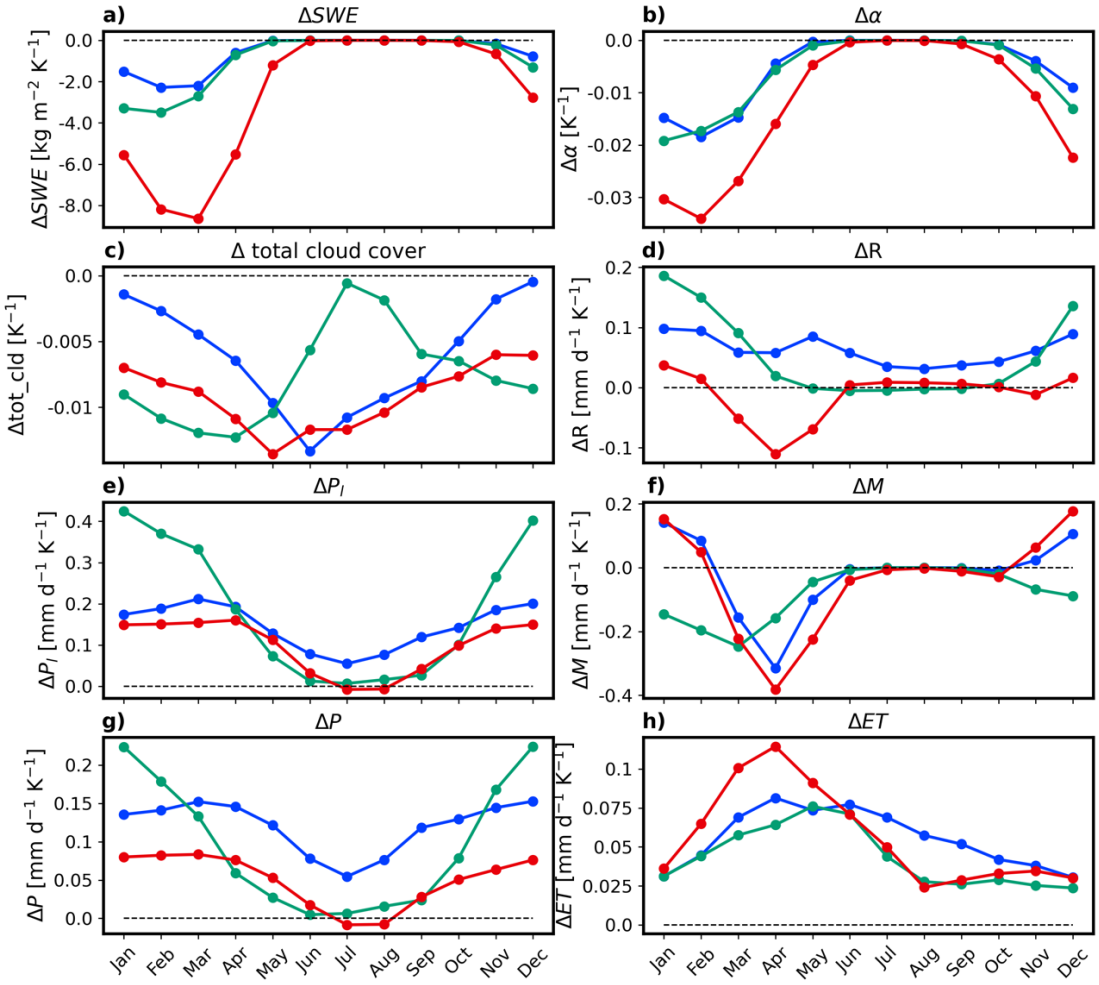

Figure S6: Seasonal dependence of absolute changes with warming in some additional hydrologically relevant metrics. a) shows snow water equivalent (SWE), b) surface albedo α, c) total cloud cover and d) runoff R, e) liquid precipitation P_l, f) melt M, g) total precipitation P and h) evapotranspiration ET.

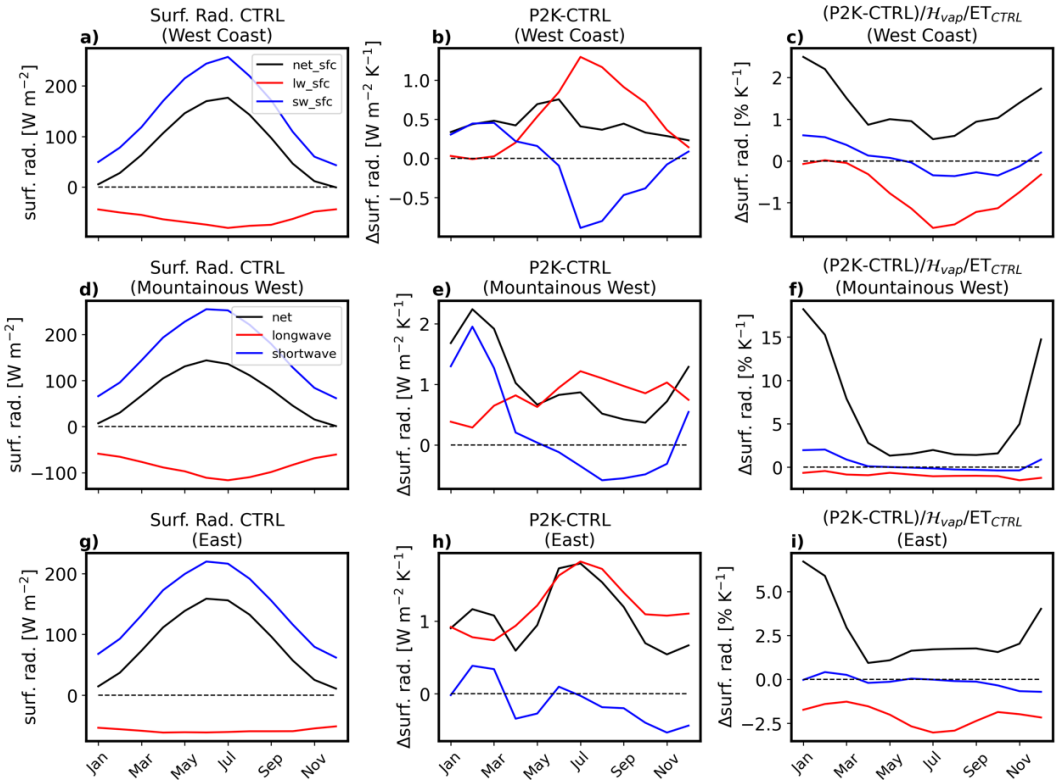

Figure S7: Mean seasonality of surface energy balance, dividing the net (black) into shortwave (blue) and longwave (red) components across the three sub-regions of CONUS, the west coast (first row), the mountainous west (second row) and the eastern US (third row). Second column shows absolute change with warming, and third column shows relative change with warming with reference to specific heat of vaporization and ET$_{CTRL}$ to achieve comparability to relative ET changes.

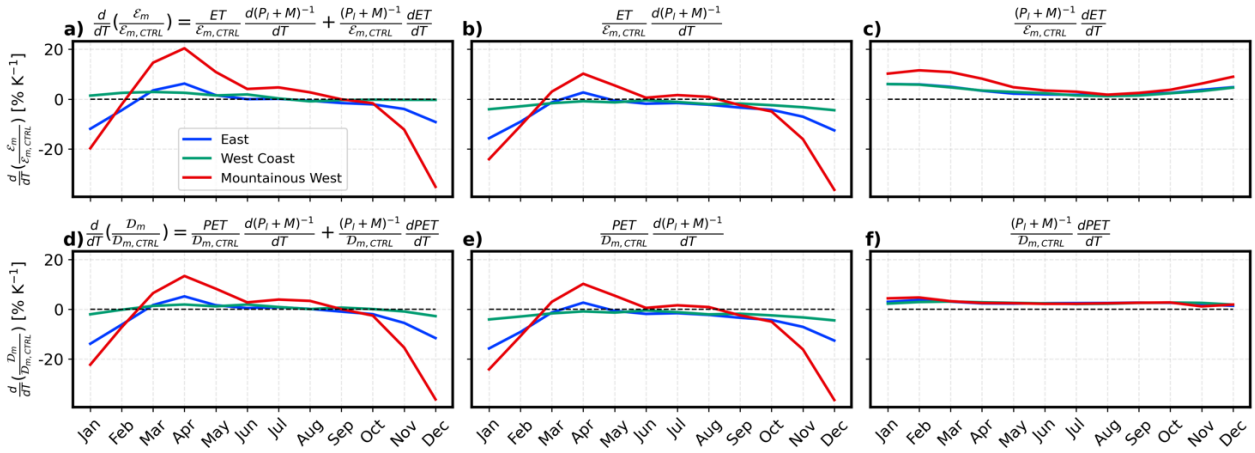

Figure S8: Seasonality of (a) change in evaporative Index $\mathcal{E} = ET/(P_l + M)$ and its decomposition into (b) changes from the denominator $(P_l + M)$ and (c) changes from the nominator (ET) for the three subregions of CONUS. Second row shows the same decomposition for the dryness Index $\mathcal{D} = PET/(P_l + M)$. The decomposition is achieved by following the product rule of derivation. The y-axis is shared among all sub-plots.

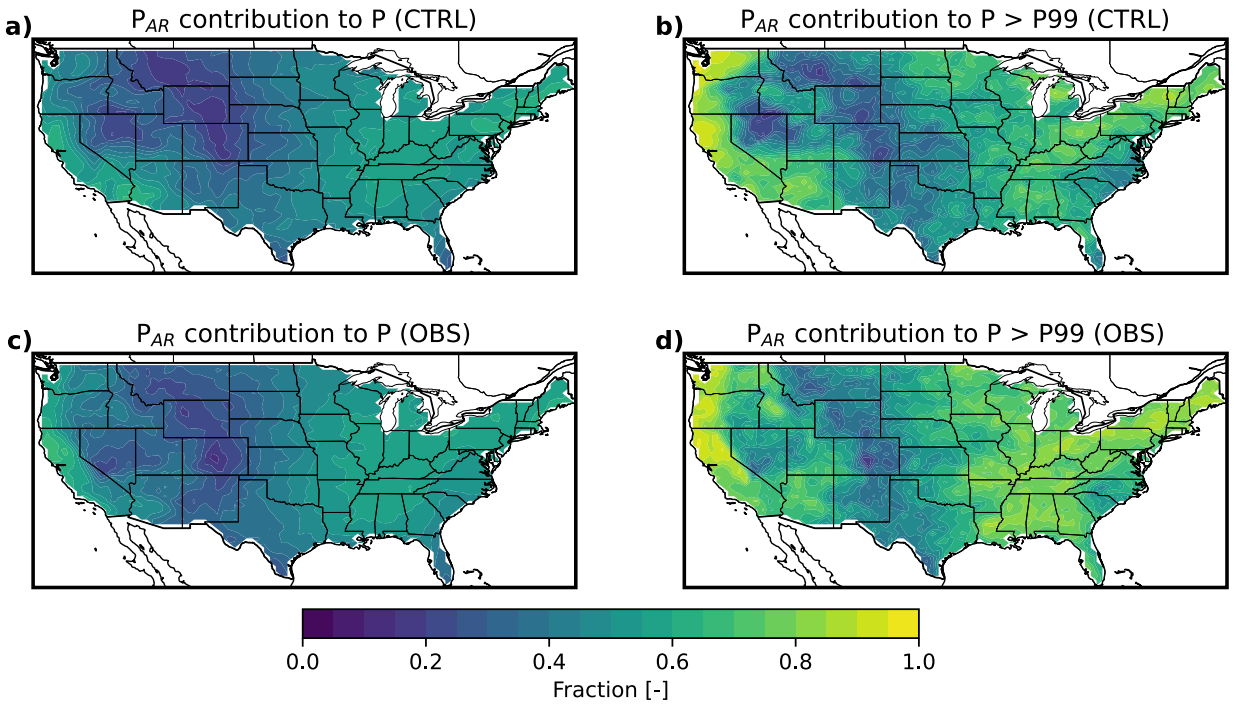

Figure S9: Contribution of AR precipitation to total precipitation (a+c) and to days exceeding 99th percentile of daily precipitation (b+d) for nudged CTRL simulation (a+b) and observations (c+d) based on IMERG precipitation and ERA5 IVT data used for AR identification.

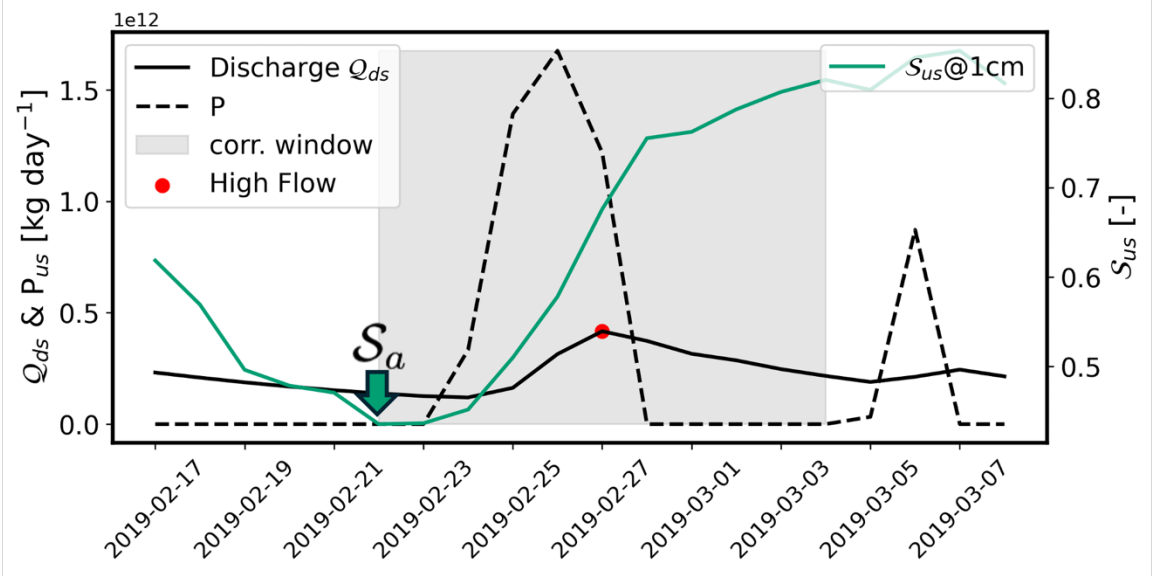

Figure S10: Example of timeseries of downstream discharge Q_{ds}, upstream area-sum of precipitation P_{us} and upstream soil saturation at 1 cm depth around a high-flow event indicated by red dot. The example is the same as the one in suppl. Fig. S5, showing the same correlation window that is determined based on τ_{drain}. The antecedent soil saturation is defined as the minimum soil saturation within the correlation window leading up to the high-flow, as indicated by the green arrow in the figure.